A Spatiotemporal exploration and 3D modeling of blood flow in healthy carotid artery bifurcation from two modalities: Ultrasound-Doppler and phase contrast MRI

Arij Debbich, Asma Ben Abdallah, Mezri Maatouk, Badii Hmida, Monica Sigovan, Patrick Clarysse, Mohamed Hédi Bedoui

A Spatiotemporal exploration and 3D modeling of blood flow in healthy carotid artery bifurcation from two modalities: Ultrasound-Doppler and phase contrast MRI*

Arij Debbich[a,b], Asma Ben Abdallah[a], Mezri Maatouk[c], Badii Hmida[c], Monica Sigovan[d], Patrick Clarysse[d] and Mohamed Hédi Bedoui[a]

[a]LTIM: Laboratory of Technology and Medical Imaging, Faculty of Medicine, University of Monastir, Tunisia
[b]National School of Engineers of Sfax, University of Sfax, Tunisia
[c]Medical Imaging Department, CHU Fattouma Bourguiba, Monastir, Tunisia
[d]Univ Lyon, INSA-Lyon, Université Claude Bernard Lyon 1, UJM-Saint Etienne, CNRS, Inserm, CREATIS UMR 5220, U1206, F-69621, LYON, France

ARTICLE INFO

Keywords:
Computational hemodynamics
Carotid bifurcation
PC-MRI
US Doppler
Normal blood flow

ABSTRACT

In the present study, we investigated the velocity profile over the carotid bifurcation in ten healthy volunteers by combining velocity measurements from two imaging modalities (PC-MRI and US-Doppler) and hemodynamic modeling in order to determine the optimal combination for the most realistic velocity estimation. The workflow includes data acquisition, velocity profile extraction at three sites (CCA, ECA and ICA), the arterial geometrical model reconstruction, a mesh generation and a rheological modeling. The results showed that US-Doppler measurements yielded higher velocity values as compared to PC-MRI (about 26% shift in CCA, 52% in ECA and 53% in ICA). This implies higher simulated velocities based on US-Doppler inlet as compared to simulated velocities based on PC-MRI inlet. Overall, PC-MRI inlet based simulations are closer to measurements than US-Doppler inlet based simulations. Moreover, the measured velocities showed that blood flow keeps a parabolic sectional profile distal from CCA, ECA and ICA, while being quite disturbed in the carotid sinus with a significant decrease in magnitude making this site very prone to atherosclerosis.

1. Introduction

Vascular maladies may be caused by thrombi and can lead to stroke [18]. Nowadays, this pathology represents a major health challenge since it is one of the leading causes of mortality all over the world (5.5 million people died of stroke in 2016) [42]. Hence, the importance of investigating the blood flow pattern, notably in the carotid artery which irrigates the brain. This artery is located in the neck. It is composed of the common carotid artery (CCA) which divides into the external carotid artery (ECA) and the internal carotid artery (ICA) irrigating the face and the brain respectively. Several in vivo [15, 16, 28, 17, 30] , in vitro [45, 21, 2], in-silico [23, 19, 49, 33, 11], and mixed image-CFD (Computational Fluid Dynamics) [22, 36] approaches have focused on this artery and associated anomalies. The investigations are mainly aimed at localizing and characterizing vessel pathologies from velocity distribution.

CFD simulation has received considerable interest owing to its ability to give access to parameters characterizing the vascular flow, not easily accessible through direct measurements, with notably Wall Shear Stress (WSS) parameters, Oscillatory Shear Index (OSI), Relative Residence Time (RRT) and helicity. Several studies have pointed the importance of having an accurate carotid geometry [7, 34]. Some studies investigated the impact of various rheological models in CFD modeling [33, 44]. Morbiducci and al. [33] suggested that if the rheological model was simplified and blood attributed a constant viscosity (Newtonian fluid) instead of a variable one (Non Newtonian), the difference in the simulations would be less than 10%. Other works [39, 7] have shown that inlet boundary conditions significantly affect the numerical simulation of velocity, which also depends on the carotid artery localization.

Blood flow analysis can confirm the presence of a local vessel anomaly, its impact on the blood flow pattern and its possible evolution [7, 26, 25, 10]. Some flow indicators such as TAWSS (time averaged wall shear stress) and OSI can help detect and localize abnormal WSS increase leading to thrombosis formation and stroke [10].

Realistic image-based patient specific CFD modeling requires the extraction of several pieces of information from medical data with at least: i) the vascular morphology from medical imaging (Computed tomography Angiography (CTA) [43] or Magnetic Resonance Imaging (MRI) [41]). ii) measurements of blood flow velocity (Ultrasound Doppler (US-Doppler) [46] or phase contrast Magnetic Resonance (PC-MRI) [41]) to provide at least arterial input functions.

Regarding the anatomy extraction, clinicians generally use CTA since it offers a higher spatial resolution than MRI and has proved its reliability [13], especially when determining a stenosis degree. As for velocity, the most widespread

*This study was conducted within the framework of the LABEX PRIMES (ANR-11-LABX-0063) project of the University of Lyon, within the "Investissements d'Avenir "(ANR-11-IDEX-0 0 07) program operated by the French National Research Agency (ANR).

arij.debbich@gmail.com (A. Debbich); assoumaba@yahoo.com (A.B. Abdallah); m.mezri@gmail.com (M. Maatouk); hmidabadii@gmail.com (B. Hmida); monica.sigovan@creatis.insa-lyon.fr (M. Sigovan); patrick.clarysse@creatis.insa-lyon.fr (P. Clarysse); MedHedi.Bedoui@fmm.rnu.tn (M.H. Bedoui)
ORCID(s):

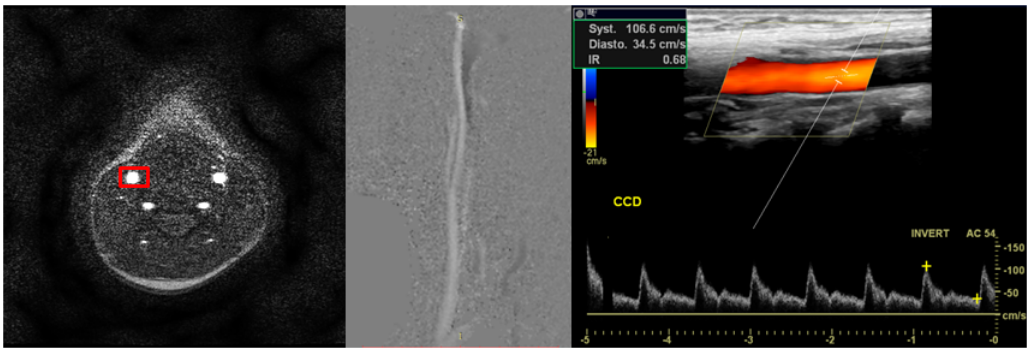

Figure 1: Medical imaging modalities to study the blood flow in the carotid artery for one of the ten subjects. Left: MRI anatomical slice transverse to the carotid arteries with the region of interest (in red), middle: PC-MRI flow slice showing the coronal component of the velocity in the carotid, which is vertically oriented, right: US-Doppler measurement showing the peak systolic velocity (PSV), the end diastolic velocity (EDV), the resistance index (top, left), the Doppler signal in the coronal cut of the CCA (top right) and the velocity profile variation in six successive cardiac cycles (bottom).

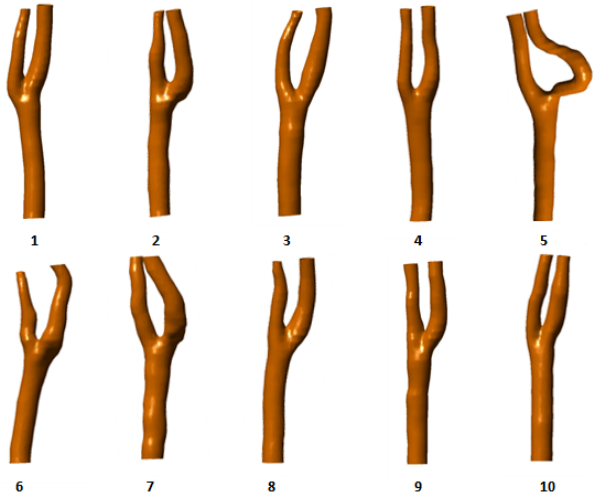

Figure 2: Reconstructed patient-specific carotid artery models for the ten subjects.

clinical assessment is based on US-Doppler because of its accessibility and its ease of use, particularly for the neck. However, this examination is operator-dependent and getting velocity values all over the carotid artery bifurcation is a hard task. This limitation may be overcome with PC-MRI which can bring both geometric and hemodynamic information simultaneously thanks to a compromise between spatial resolution and acquisition time. In this context, few studies compared velocity measurements in the carotid artery between US-Doppler and PC-MRI [15, 16, 38, 28]. They showed that there was a significant variation of velocity values in the CCA and that PC-MRI generally leads to smaller velocity values compared with US-Doppler. However, these studies have not considered CFD simulations to complete measurement characteristics in order to obtain an overall carotid hemodynamic exploration.

In this paper, our objective is to design an optimized patient specific CFD workflow in terms of quality of velocity profiles, computational efficiency and clinical applicability. The anatomical data are obtained from PC-MRI, while velocity data are obtained from both PC-MRI and US-Doppler. This allows us to address two sub-goals i) comparing velocity measurements from the two imaging modalities implying different acquisition conditions (the widespread US-Doppler, and less routine PC-MRI) and providing different velocity quantifications (1D-axial vs 3D). ii) investigating the optimal combination of velocity measurements and CFD modeling to provide realistic patient specific flow simulations. We investigated and modeled blood flow velocity from imaging data in ten healthy volunteers. This work may also allow deriving PC-MRI and/or US-Doppler measured velocities given numerical velocities. Section 2 describes the imaging data sets and the analysis methodology. Section 3 presents the obtained results that are discussed in section 4.

2. Material and Methods

The arterial geometrical model was extracted from MR anatomical images and the hemodynamic modeling was performed from the obtained models. The velocity waveforms from both PC-MRI and US-Doppler were extracted at three locations: the right CCA, ECA and ICA.

2.1. Imaging Data

Right carotid artery bifurcations in 10 healthy volunteers (4 males and 6 females, median age: 35 years, range: 24-57 years) with no cardiovascular disease history, were explored at the Radiology Department of Fattouma Bourguiba University Hospital using both PC-MRI and US-Doppler according to the following protocols.

2.1.1. PC-MR imaging

The PC-MR images were acquired with a clinical 1.5 T Philips system (Ingenia, Philips medical systems, Best, the Netherlands) using 20 channels phased array head neck spine coil. Two acquisitions (anatomical and flow imaging) were performed (Figure 1). Fifty 2D anatomical images were acquired in axial orientation to cover cervical region

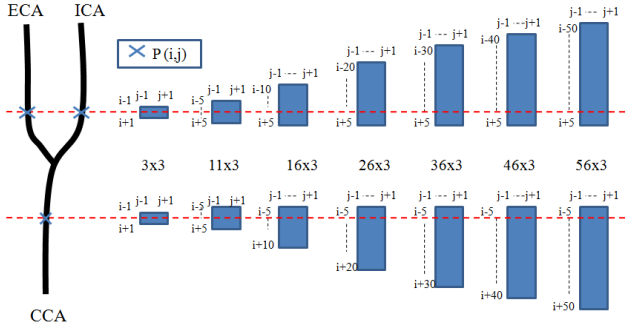

Figure 3: Growing carotid scanning windows size. Key points are located in: CCA at 1.5 cm from the bifurcation, ECA and ICA: at 1 cm from the bifurcation.

with T1 Fast Field Echo (T1 FFE) and the following parameters: Repetition time (TR)=13 ms, echo time (TE)=3.6 ms, NEX (signal average)=1, flip angle=60 deg, pixel size=0.44 x 0.44 mm, slice thickness=3 mm, GAP=2 mm.

The images obtained were then used to acquire four flow images in oblique sagittal plane (including right carotid bifurcation with most of CCA and ICA) using 3D Phase Contrast Angiography (PCA) and the following parameters: TR=11 ms, TE=7.1 ms, flip angle=15 deg, pixel size=0.73 x 0.73 mm^2, slice thickness=3 mm, NEX=1, velocity encoding (VENC)=90 cm per sec, retrospective cardiac gating based on pulse oximeterplethysmography was used and 14 phases of cardiac cycle were acquired. The ideal velocity encoding (VENC) should be high enough to avoid aliasing and as low as possible to reduce velocity noise [47]. Since velocity in the carotid artery for normal subjects does not generally go over 110 cm/s and rarely exceeds 90 cm/s, we fixed VENC at 90 cm/s.

To minimize the acquisition time, we restricted VENC to the cranio-caudal direction only. This approach modifies neither temporal nor spatial resolution. However, it allows the reduction of acquisition time by a factor of 3. The total scan time for an exam was approximately 7 minutes.

2.1.2. US-Doppler imaging

All US-Doppler exams were conducted by a radiologist (B.H) with 10 years' experience in cardiovascular imaging. Clinical General Electric ultrasound systems (LOGIQ E9, GE Healthcare, Milwaukee, WI, USA) with 9 MHz linear probe were used. For each subject, velocity profiles of the right carotid bifurcation were recorded at the following locations:

• CCA: 1.5 cm from the carotid sinus

• ECA and ICA: 1 cm from the carotid sinus except the ICA of volunteer number 5 since his carotid morphology was specific.

US-Doppler images were matrices of dimension 720x960. To extract the velocity waveform, we chose a profile of one cardiac cycle (Figure 1-right-bottom), fixed the two profile axes and selected 14 feature points on these profiles including PSV and EDV. A cubic spline interpolation of these

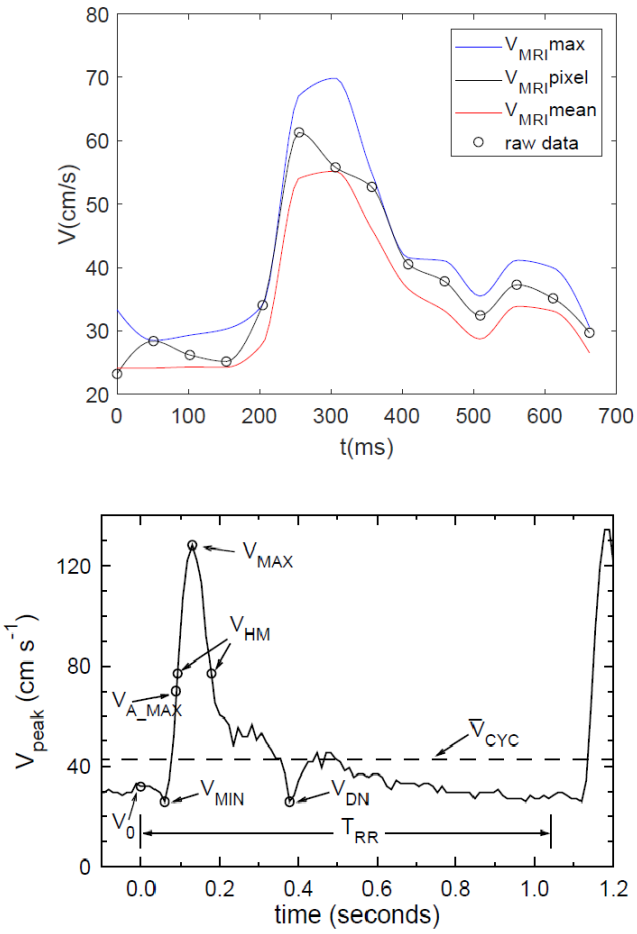

Figure 4: CCA velocity waveform extracted from MRI data (VMRImax, VMRImean and VMRIpixel) for Volunteer 1 (top) and feature points of CCA velocity waveform extracted from US data in [17] (bottom).

points provided the US-Doppler velocity profile. The US-Doppler profile point digitization was performed using the Engauge Digitizer software [29].

2.2. PC-MRI Velocity profile extraction

Three velocity waveforms were extracted from PC-MRI at locations CCA, ECA, and ICA during a cardiac cycle which was divided into 14 time points. The following values were deduced from the interpolated waveforms:

- Velocity variation at a given pixel $V_{MRIpixel}$ (See Algorithm in the Appendix).
- Maximum velocity at a given pixel within its eight neighbors V_{MRImax}.
- Mean velocity at a given pixel within its eight neighbors $V_{MRImean}$ Velocity profile processing was performed using MATLAB R2017 b. The PC-MRI waveforms ($V_{MRIpixel}$, V_{MRImax}, $V_{MRImean}$) were compared to the US-Doppler velocity waveforms V_{US} and to the CFD simulated waveforms V_{SIM} located at the same sites of the vessel. Comparison of the measured velocities between US-Doppler and MRI re-

quires the two waveforms to be temporally aligned: starting at the same point of the cardiac cycle and focusing the evaluation on the same time interval for both modalities. However, as the MRI and the US-Doppler examinations were not acquired at the same time, there might be some physiological variations [16]. To minimize this effect, the 14 velocity values from PC-MRI were temporally aligned to the 14 extracted points of the US-Doppler curve based on key time points (where t/T=0, 0.07, 0.15, 0.23, 0.3, 0.38, 0.46, 0.53, 0.65, 0.69, 0.76, 0.84, 0,92, 1).

2.3. Arterial model reconstruction and computational mesh generation

Out of 50 cross sections of MR imaging data, we selected 32 sections to be segmented: 18 sections before the bifurcation related to CCA and 14 sections after the bifurcation related to ICA and ECA, to obtain a common size for all the geometrical models with 3.3 cm of CCA length and 2.5 cm of ECA and ICA length after cutting the wall ends and creating the inlet/outlet surfaces. The geometrical characteristics of all the vessel segments for the ten subjects are given in Table1. The carotid lumen was separated from the rest of the structures by applying an intensity threshold. In some cases, for instance in the case of subject movement, an expert corrected manually the segmentation. The 3D arterial model was constructed using a Marching Cubes algorithm [27] leading to a triangular surface mesh which was further re-meshed if necessary, in order to respect an imposed number of facets per surface unit [4] and therefore ensure a high mesh quality for the CFD simulations. Then, we imported the 3D wall model to create the inlet/outlet surfaces. The model was further re-meshed using an Octree surface refinement based on prismatic wall [20]. Next, a volumetric meshing was generated based on the Delaunay tetrahedral refinement algorithm [53]. The segmentation and the image-based 3D mesh reconstruction steps were performed using the AMIRA [1] software. The border surface creation was done using DESIGN MODELER software and the mesh refinement was performed by ICEM, both from ANSYS [2]software. The obtained geometrical models for the 10 subjects are displayed in Figure 2. Blood flow modeling was based on computational fluid dynamic (CFD) to solve the governing equations through the finite volume method (FVM) targeting partial differential equations solving. As blood is an incompressible fluid with a non-Newtonian behavior and given that all considered geometries belong to healthy subjects without anomalies like stenosis or aneurisms, we chose the Navier-Stokes equation for incompressible fluid with a laminar flow described by the following equations [1]:

$$\rho\left(\frac{\partial v}{\partial t} + (v.\nabla)v\right) = -\nabla p + \mu\nabla^2 v \quad (1)$$

$$\nabla.v = 0 \quad (2)$$

[1]Thermo Fisher Scientific and Zuse Institute Berlin (ZIB)
[2]ANSYS, Inc, Canonsburg, USA

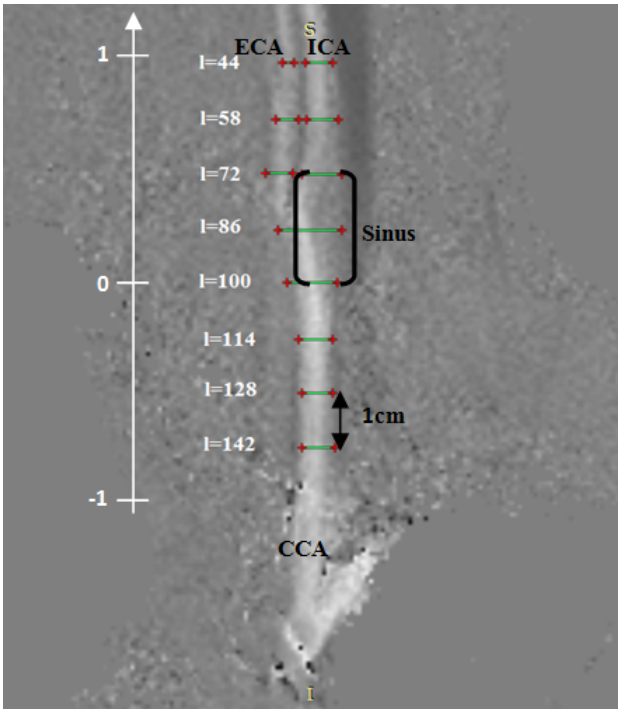

Figure 5: Localization of extracted velocity profiles along the carotid bifurcation in the coronal orientation of PC-MRI data (Volunteer 1). One cm of vessel length corresponds to 14 pixels.

where v is the velocity, t the time, ρ the density, p the pressure and μ the dynamic viscosity.

Some studies adopted the rheological Newtonian behavior for the carotid artery (stationary viscosity) because it is simpler than the hemodynamic modeling with a non Newtonian behavior and arguing it has a minor impact on the results [33]. In this study, we kept the non-Newtonian property for blood flow modeling to stay closer to reality. We considered the Herschal-Bulkley condition, which defines viscosity properties as in [51]:

$$\mu = k\dot{\gamma}^{n-1} + \frac{\tau_0}{\dot{\gamma}} \quad (3)$$

$$\dot{\gamma} = \nabla v + (\nabla v)^T \quad (4)$$

where k is the consistence index, n the power low index, τ_0 the yield stress threshold (k=0.01 Kg/m s, n=0.68, τ_0=0.4 Pa) and $\dot{\gamma}$ the rate of strain tensor.

2.4. Boundary conditions

One of our objectives was to investigate the impact of the inlet boundary conditions on the simulation results. Therefore, blood flow modeling was studied with two velocity inlets: PC-MRI and US-Doppler velocity waveforms extracted at the CCA location. These inlets were pulsed over time and were composed of the two usual physiological phases during a cardiac cycle: systole and diastole. The PC-MRI inlet

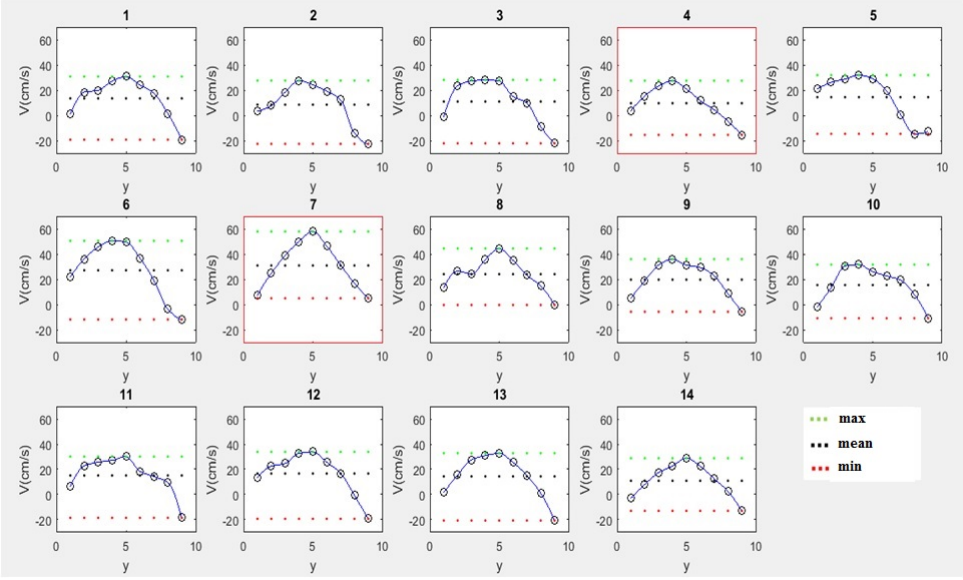

Figure 6: Spatiotemporal velocity profile evolution in the CCA diameter (3.3 cm before bifurcation, l=128 according to Figure 5) at the 14 time points of the cardiac cycle according to PC-MRI data of volunteer 1. End-diastole and peak systole correspond to time points 4 and 7 respectively.

velocity profile for every subject was matched to V_{MRImax} in the CCA, 3.3 cm from the carotid bifurcation to conform to the CCA dimension in the geometrical model. Due to experimental constraints, velocity measures 1.5 cm proximal to the bulb V_{US} were considered as US-based inlet velocity.

The inlet velocity profile is pulsed over time and spatially parabolic through a User Defined Function (UDF) from Ansys sofware over the vessel section:

$$v_t = h_t \left[1 - \left(\frac{(x - x_c)^2 + (y - y_c)^2}{R^2} \right) \right] \tag{5}$$

where h_t is the maximal parabolic magnitude matching the V_{MRImax} or V_{US} at time t. (x_c, y_c) and R are respectively the center coordinates and the radius of the CCA inlet section. We chose a parabolic profile inlet instead of a Womersley profile inlet although the latter is often used. A comparative study between different inlets (parabolic, blunt and Womersley) showed that WSS and OSI of simulations based on parabolic inputs were closest to those based on patient specific inlet velocity profiles [7]. The vessel walls were assumed to be rigid and the flow ratio was set to 60% and 40% of the CCA flow in the ICA and ECA respectively [50, 32]. As in many previous works, we chose a constant flow ratio of 60:40 throughout the cardiac cycle for all volunteers to simplify boundary conditions in case the carotid arteries were healthy.

A grid dependency study based on three meshes with increasing number of control volumes (222 015, 281 622 and 415 589) was established. All meshes brought velocity profiles close to each other. We chose the intermediate one as a good compromise between accurate estimation and reduced computing time.

2.5. Simulated velocity profiles

Simulated velocity profiles V_{sim} were extracted at three locations of the carotid bifurcation: 1.5 cm from the bifurcation in the CCA and 1 cm up the bifurcation in ECA and ICA. The values were extracted using CFD-POST from ANSYS software.

3. Results

Velocity waveforms were extracted from PC-MRI (V_{MRImax}, $V_{MRIpixel}$ and $V_{MRImean}$) and Doppler-US (V_{US}) imaging data for ten volunteers at the three localizations of the carotid artery. Two velocity profiles were simulated. The first one, called V_{SIM_MRI}, is based on PC-MRI data V_{MRImax} profile used as inlet boundary condition. The second one, termed V_{sim_US}, results from a simulation with V_{US} profile as inlet boundary condition. All velocity waveforms characteristics are reported in the Appendix (Tables 2 (CCA), 3 (ECA) and 4 (ICA)). We did not integrate the pixel-based PC-MRI velocity $V_{MRIpixel}$ in the tables since its values were between those of V_{MRImax} and $V_{MRImean}$ and were noisier.

To assess the quality of our model, we compared the simulated velocity waveforms with the measured ones in three vessel segments using three indicators. The first indicator is a global one that calculates the normalized Root Mean Squared Error (RMSE) between the measured (*meas*) and the numerical (*num*) values of the velocity profiles [4, 55, 3]:

$$\varepsilon_v = \frac{1}{N} \sum_{i=1}^{N} \frac{\sqrt{(v_i^{meas} - v_i^{num})^2}}{max(v^{meas})} \tag{6}$$

where N is the number of instants in a cardiac cycle (N=14). Two other indicators focused on the Peak Systolic Velocity

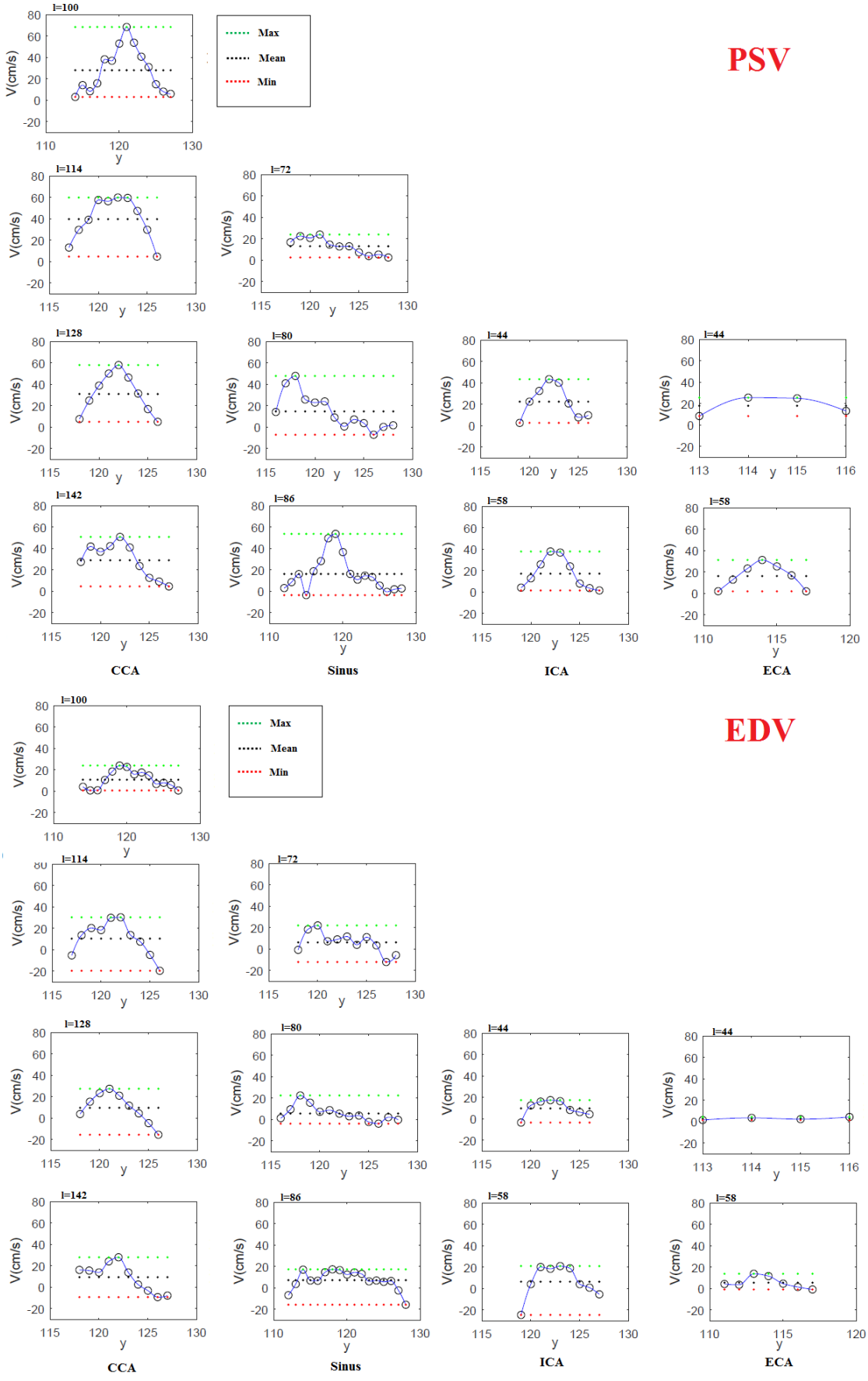

Figure 7: PSV and EDV profiles at several levels (see Figure 5) of the bifurcation carotid artery according to PC-MRI data for Volunteer 1.

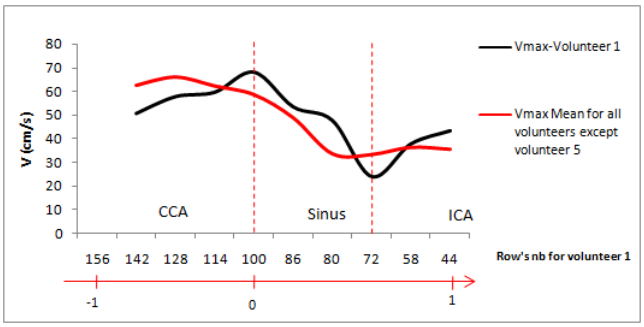

Figure 8: Vmax at the peak systolic time point according to PC-MRI data along the carotid bifurcation of Volunteer 1 and Vmax mean of 9 volunteers (all except #5) in the same conditions (PSV according to PC-MRI data). The range [-1,1] represents the axis encompassing the carotid bifurcation from CCA to ICA (see Figure 5).

(PSV) and the End Diastolic Velocity (EDV) respectively. They estimated the relative difference between numerical and in vivo values at these two instants [55]:

$$\gamma_{PSV} = \frac{\|PSV^{meas} - PSV^{num}\|}{PSV^{meas}} \quad (7)$$

$$\gamma_{EDV} = \frac{\|EDV^{meas} - EDV^{num}\|}{EDV^{meas}} \quad (8)$$

These local metrics are generally expressed in percentage change and tend towards zero when the measured and numerical values present a low difference.
The values obtained for the 10 cases are given in the Appendix (Tables 5 ,6 and 7 for CCA, ECA and ICA respectively).

3.1. Analysis of PC-MRI velocities

Typical measured velocity waveforms from PC-MRI are presented in Figure 4. They were in accordance with conventional CCA velocity waveform. They all presented the main feature points that could be found in a CCA profile as described in Figure 4- bottom [17].

For PC-MRI data of one volunteer, we studied V_{MRImax} velocity along bifurcation carotid artery at 14 instants within a window of increasing size: 3x3, 11x3, 16x3, 26x3, 36x3, 46x3 and 56x3 pixels (Figure 3). These windows were taken at the following locations: 1 cm from the bifurcation in the ICA and ECA and 1.5 cm from the bifurcation in CCA. We noted that velocity increases with window size until reaching a maximum value for each vessel segment with size 46x3: 75 cm/s in CCA, 44 cm/s in ICA and 50 cm/s in ECA. These results correlations were in accordance with the values in Tables 2, 3, and 4 in the Appendix in which the mean of V_{MRImax} values for 10 subjects within a 3x3 window size are as follows: 61 cm/s in CCA, 48 cm/s in ECA and 35 cm/s in ICA. This quantification gives a ratio of blood flow velocity in ICA to CCA, V_{ICA}/V_{CCA} of 0.58 and 0.57 for 46x3 and 3x3 window size respectively. This value was lower than those

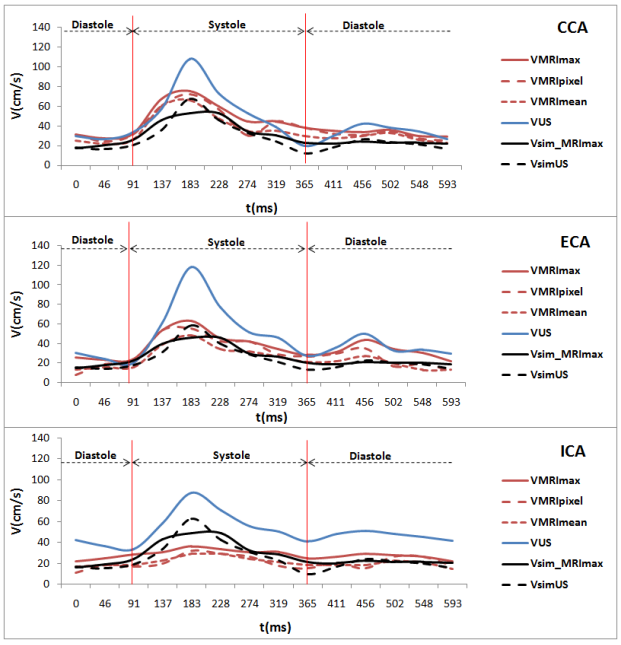

Figure 9: Measured and numerical velocity waveforms of CCA, ECA and ICA for volunteer # 10.

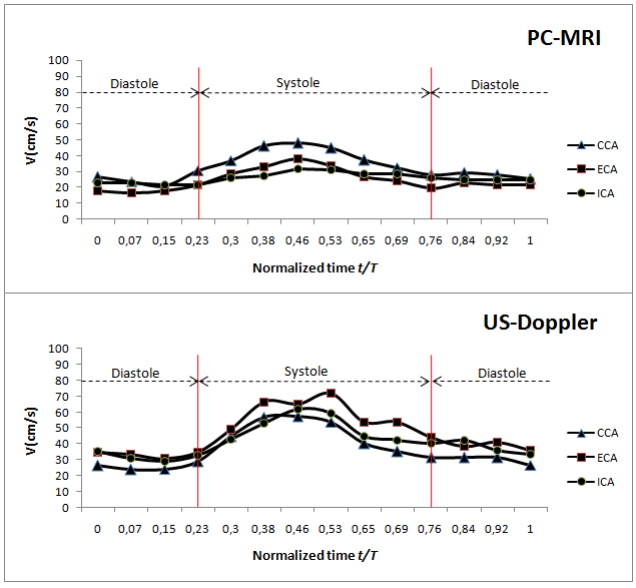

Figure 10: Mean velocity for the 10 normal subjects in CCA, ECA and ICA relative to V_{MRImax} for PC-MRI (up) and V_{US} for US-Doppler (down).

found in similar studies dealing with normal subjects: 0.7 in [31] (mean ratio of 7 healthy subjects with US-Doppler) and 0.81 in [24] (343 subjects examined with US-Doppler). It should be noted that a ratio equal or superior to 1.4 is clinically interpreted as a stenosis of more than 50% [48].

We noted that a velocity profile over the CCA diameter at a given location (3,3 cm before bifurcation, l=128, Figure 5) was almost parabolic for all time points (Figure 6). To investigate the profile shape all over the carotid bifurcation, we extracted the diameter profile for the peak systolic (PS)

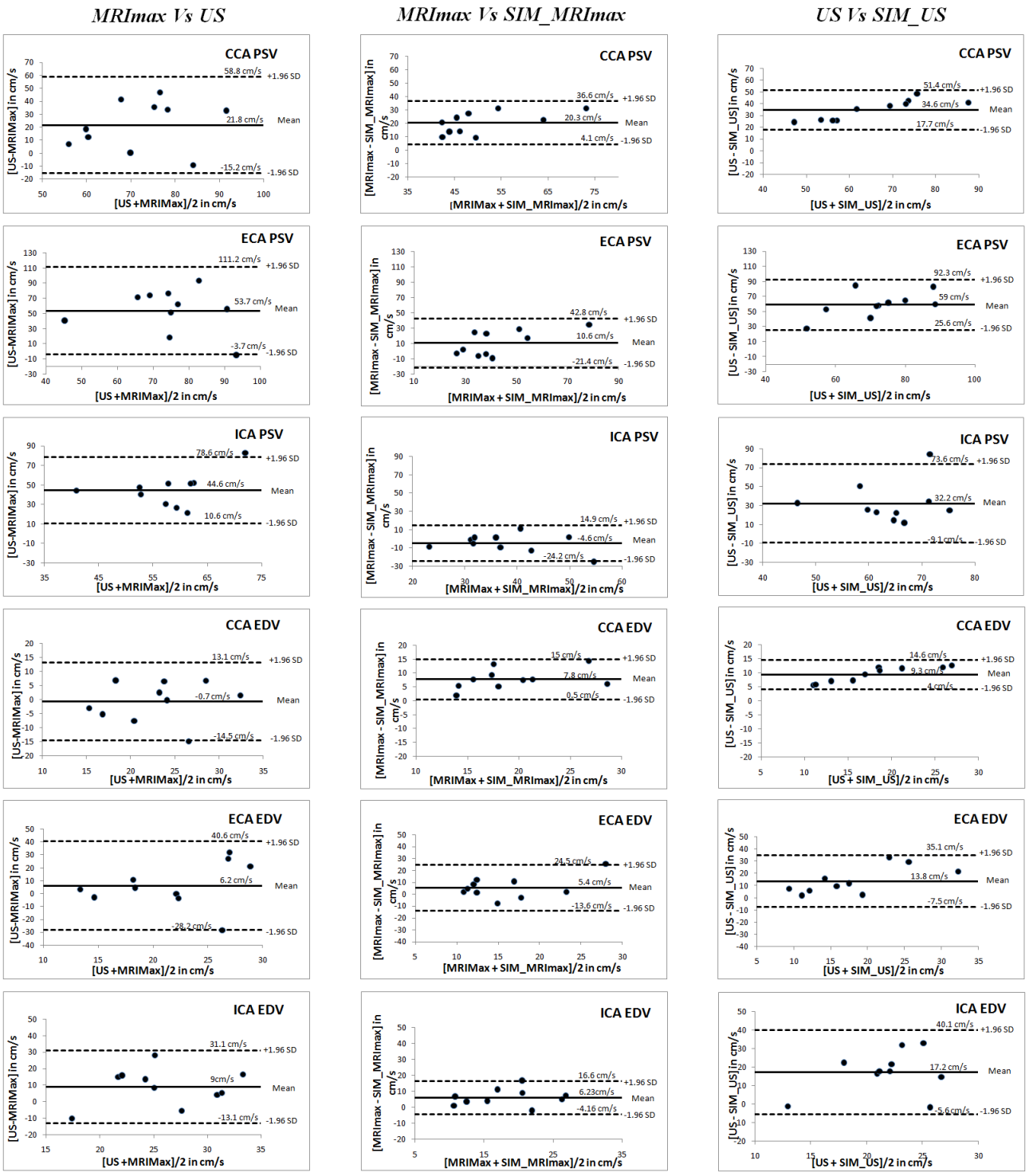

Figure 11: Bland-Altman plots of PSV and EDV comparing simulation and measurements for CCA, ECA and ICA. Left: PC-MRI vs US-Doppler, Middle: PC-MRI vs simulation SIM-MRImax. Right: US vs simulations SIM-US. PSV and EDV were compared for 10 right carotid bifurcations in 10 normal volunteers.

and end diastolic (ED) time points every centimeter from the CCA to the carotid sinus, ICA and ECA (Figure 7).

We noticed that the PSV and EDV velocity profiles had almost a parabolic shape with small variations in CCA, ICA and ECA (Figure 7). There were significant variations detected in the carotid sinus site: a progressive decrease of the maximum velocity and a disruption of the profile shape. This was an expected result since the carotid sinus presents the biggest wall volume in the bifurcation carotid artery. This velocity variation led to a WSS decrease, which could

make this zone very sensitive to atherosclerosis [35].

From the profiles shown in Figure 7, we extracted the maximum velocity V_{max} at peak systole time with one centimeter step from CCA passing through the sinus to ICA in the PC-MRI image. We started from location l=142 corresponding to CCA up to l=44 corresponding to ICA. Velocity evolution was correlated with the artery localization (Figure 8) with an increase phase over the CCA, a decrease phase over the sinus and an increase phase in the ICA. This was caused by the geometry variations in the carotid bifurcation. The decreasing velocity behavior in the sinus was similar among all normal subjects (except #5 which presented an atypical shape, see Figure 2) as also shown with the mean velocity profile among the cases (red curve in Figure 8). However, the mean velocity in CCA and ICA remained almost constant.

3.2. Analysis of PC-MRI and US velocity measurements

According to Table 2 in the Appendix, the mean US-Doppler PSV of 10 subjects in CCA was higher than the maximum mean PC-MRI PSV by about 26% (83 cm/s for V_{US} vs 61 cm/s for V_{MRImax}) and the mean PC-MRI PSV by about 36% (83 cm/s for V_{US} vs 53 cm/s for $V_{MRImean}$). This is in the range of differences observed in previous works that found shifts of about 24% [38], 26% [16], 33% [14] and 25.9% [15]. This difference exists partially because of the lower temporal and spatial resolution of the MRI modality compared to US [15, 16, 54].

This difference between US-Doppler and PC-MRI values increases for ECA and ICA (52.8% in ECA and 53.8% in ICA according to V_{US} and V_{MRImax} values, Tables 3 and 4 in the Appendix). Unlike the difference observed by Harloff et al.[15] for ICA, PSV of PC-MRI was on average less than US-Doppler by about 17.6%. This can be partly due to the difference between the 1D-Feet-Head velocity used in this study and the 3-component velocity. For PSV, we estimated a mean dissimilarity between 1D-Feat-Head and 3D-velocity of 0.8% in CCA, 4.6% in ICA and 3.7% in ECA. For EDV, the difference between US-Doppler and PC-MRI for V_{MRImax} was about 3% for CCA, 24% for ECA and 26% for ICA.

The comparison between PSV and EDV of PC-MRI (V_{MRImax}) and US-Doppler (V_{US}) was further assessed using the Bland and Altman plots [5] (Figure 11-*MRImax* Vs *US*). PSV from MRI was clearly lower than PSV measured using US-Doppler in both ECA and ICA (mean difference of 53.7 cm/s and 44.6 cm/s respectively). The shift observed for EDV was 6 cm/s and 9 cm/s in ECA and ICA respectively. The same tendency was observed in CCA PSV (mean difference of 21.8 cm/s), to a much lower extent for CCA EDV (-0.7 cm/s of mean difference, Figure 11-*MRImax* Vs US).

Figure 9 shows the different velocity waveforms of volunteer 10 in CCA, ECA and ICA obtained from PC-MRI (red), US-Doppler measurement (blue) and simulation (black). According to this figure, the three PC-MRI waveforms (V_{MRImax}, $V_{MRImean}$, $V_{MRIpixel}$) are very close to each other. The systolic velocity profiles for US-Doppler and PC-MRI are significantly different especially in ECA and ICA. Diastolic velocity profiles are less dissimilar except in ICA for the two modalities.

The mean velocity waveforms of the ten volunteers relative to PC-MRI and US-Doppler in CCA, ECA and ICA are plotted in Figure 10. The time dimension was normalized with respect to the cardiac cycle. The figure shows the clear difference in magnitude between PC-MRI and US-Doppler velocities. The three PC-MRI velocity waveforms exhibit a standard behavior, comparable with other PC-MRI measurements reported in [8, 31]. The mean profile of US-Doppler velocity waveforms in ECA presents an atypical behavior compared to the ones in normal subjects. The ECA amplitude exceeded those of CCA and ICA, which differs from usual US-Doppler waveforms like those used as inlet boundary conditions in [9].

3.3. Analysis of simulated velocity waveforms

Overall, the numerical velocity waveforms were closer to the PC-MRI ones independent of the arterial input function considered (US or MRI). The numerical velocities were compared to *in vivo* measurements through the global and the local indicators defined in section 3 (Tables 5, 6 and 7 in the Appendix). V_{SIM_MRImax} was compared to V_{MRImax} and V_{SIM_US} to V_{US}. The results showed that real and simulated velocity waveforms exhibited the same shape and respected the physiological phase variations during the cardiac cycle (Figure 9). The average between measured and simulated waveforms of the global error indicator revealed an acceptable difference: RMSE was equal to 18% and 17% in CCA, 13% and 26% in ECA and 22% and 23% in ICA (ϵ_v metric in the Appendix, Tables 5, 6 and 7). However, the mean difference between measurements and simulation for PSV and EDV was greater. For PSV, we had: γ_{PSV} = 32% and 38% in CCA, 27% and 58% in ECA and 22% and 38% in ICA; and for EDV: γ_{EDV} =32% and 38% in CCA, 37% and 47% in ECA and 29% and 53% in ICA respectively (see γ_{PSV} and γ_{EDV} metrics, Tables 5, 6 and 7).

Simulation based on PC-MRI data led to a more realistic response compared to that based on US-Doppler at the three locations. The PSV average error γ_{PSV} was 32% in CCA, 27% in ECA and 22% in ICA for PC-MRI vs 38%, 58% and 38% for CCA, ECA and ICA respectively for US-Doppler (Tables 5, 6 and 7 in the Appendix). From Tables 2, 3 and 4, it can be noted that the mean PSV of the ten subjects from V_{SIM_MRImax} is lower than that from V_{SIM_US}. This is mostly explained by the overall magnitude of PC-MRI against US-Doppler PSV measurements. The mean EDV values for the ten subjects of V_{SIM_US} and V_{SIM_MRImax} were very close in the three vessels. This is because of the proximity of V_{MRImax} and V_{US} values. The results showed that numerical velocities were highly influenced by the velocity inlet as already observed in other investigations [39].

PSV and EDV values between simulations and measurements were further compared using Bland and Altman plots (Figure 11). The results showed that the differences between

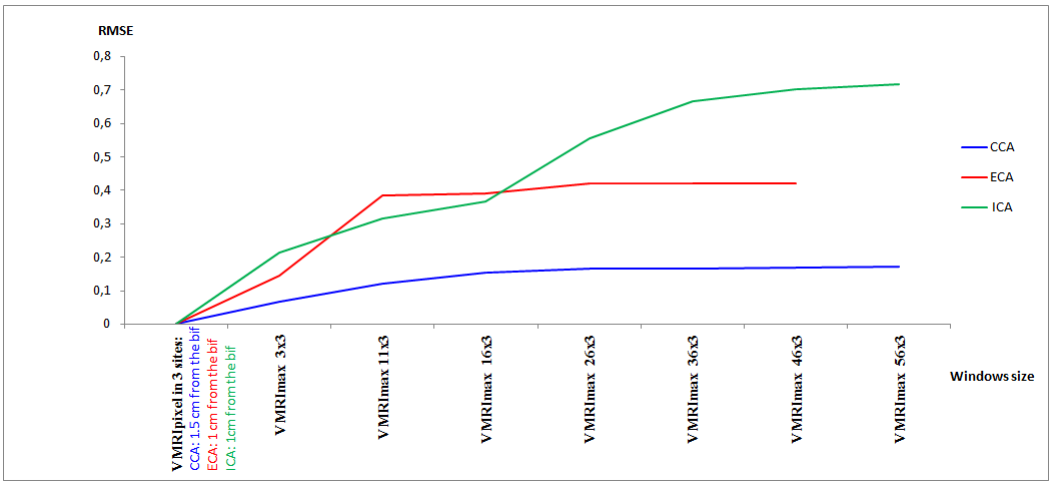

Figure 12: Velocity difference between Vpixel located at the three key sites in CCA, ECA and ICA and VMRImax over the windows size for Volunteer 1.

V_{SIM_MRImax} and V_{MRImax} were clearly smaller than those between V_{SIM_US} and V_{US} for both PSV and EDV.
Within this set of 10 cases, the mean differences between V_{SIM_MRImax} and V_{MRImax} ranged from -4.6 cm/s (ICA PSV) to +20 cm/s (CCA PSV). However, the mean differences between V_{SIM_US} and V_{US} extended from 9.3 cm/s (CCA EDV) to 59 cm/s (ECA PSV).

4. Discussion

In this study, the PC-MRI velocity behavior in the carotid bifurcation was investigated in time and space. It was observed that the velocity estimation increased with the window size up to maximum (46x3, Figure 3). We calculated the global velocity difference between V_{pixel} located in the three key sites mentioned before (Figure 3) and V_{MRImax} according to each window size (Figure 12). We found that for the three arteries, the velocity difference presented a piecewise linear growth before stabilizing. This can lead to errors in studies which compare velocity measurement techniques. That is why we recommend measurement locations should be taken in the following intervals of stability:
- In CCA, about [27 , 55] mm (∼ [4.6 , 9.3] of CCA diameter) before bifurcation,
- In ECA, about [18 , 43] mm (∼ [3 , 7.3] of CCA diameter) after bifurcation and
- In ICA, about [37 , 50] mm (∼ [6.3 , 8.5] of CCA diameter) after bifurcation.
However, this can be difficult to achieve when dealing with a PC-MRI and US-Doppler comparative study like ours for two reasons related to US measurements: i) lack of convenient accessibility for radiologists. ii) different neck size from one volunteer to another. In fact, it was not always easy to measure beyond bifurcation in subjects with reduced neck length.

In this context, to have an idea about the stability evolution of velocity along the carotid bifurcation for US-Doppler together with PC-MRI, we repeated the US measurements for volunteers 1, 3 and 4, at the following carotid artery locations:
- In CCA: 1.5, 2.5 and 3 cm from bifurcation,
- In ICA: 1, 2 and 3 cm of bifurcation.
The US-based results were in accordance with PC-MRI measurements. The systolic peak velocity value in CCA did not show a significant variation for the three volunteers. In ICA, the peak systolic velocity showed a significant increase for volunteer 3. Therefore, a compromise had to be made for the choice of the measurement site between the lowest possible position of the ICA for measurement accessibility and the farthest position to the bulb in order to ensure velocity stability.

Besides the lack of references, a detailed measurement of cross-sectional velocity profiles is still challenging. Our PC-MRI based measurements show that away from the bulb (over ∼ 1.4 cm or 2.4 of CCA diameter) the axial velocity distribution is almost parabolic (Figure 6 and 7). Within the bulb area velocity cross-sectional profiles are shown according to the division of the flow at bifurcation. This observation agrees with several CFD simulations in previous works [37, 40, 11, 12].

In this work, the arterial wall pulsatility has not been considered as it would have brought many additional issues with less mastered modeling methods (Fluid Structure Interaction). From Figure 6, the CCA geometric variation between peak systole and end-diastole can be estimated to about two pixels in volunteer 1. The integration of this aspect would require a higher anatomical resolution. This is certainly one of the future improvements to address although this might have less impact in other vessels [52]. Augmentation of both spatial and temporal resolutions can be considered with higher field (3T) MRI.

Comparing PC-MRI and US-Doppler velocity measurements, our results showed that the shift between these two measurements in CCA (26%) was similar to other studies:

about 24% in [38], 26% in [15, 16], and even 33% in [14]. However, this shift increased in ECA and ICA (about 53%). This could be attributed mainly to the use of Feat-Head velocity only. One other source of error could be the location of the US measurement in ECA and ICA (approximately 1 cm downstream of the bifurcation). It was difficult to insure that the location of US-Doppler measurements was exactly the same one as that of PC-MRI for all volunteers.

From the similarity assessment using the global indicator, we noted that V_{SIM_MRImax} and V_{SIM_US} showed a similar difference (Tables 5, 6 and 7 in the Appendix) to measurements in CCA (18% vs 17%) and in ICA (22% vs 23%), with an exception for ECA (13% vs 26%). This result suggests that PC-MRI-based hemodynamic simulations have a better global behavior, especially in ECA.

Locally, the mean difference between V_{SIM_MRImax} and V_{MRImax} varied from 22% to 32% according to the local difference metric at peak systole γ_{PSV} and from 29% to 37% according to the local difference metric at end diastole γ_{EDV} (Tables 5, 6 and 7 in the Appendix). However, the mean difference between V_{SIM_US} and V_{US} varied from 38% to 58% under PSV metric and from 38% to 53% under EDV metric. These results tend to make PC-MRI-based blood flow modeling a realistic approach in the analysis of blood flow in the carotid bifurcation.

Further application of this approach in multiple cases may additionally lead to learning a transfer function between simulated and measured (US-Doppler, PC-MRI) velocities, therefore allowing to derive missing information on the basis of available data. When correctly tuned, the CFD approach gives access to additional parameters, not currently accessible, to characterize more accurately the vascular flow through e.g. Wall Shear Stress (WSS) parameter, Oscillatory Shear Index (OSI), Relative Residence Time (RRT) and helicity.

5. Conclusion

In this paper, we investigated blood velocity quantification over the carotid artery bifurcation from PC-MRI and US-Doppler, and 3D velocity modeling from these modalities. We performed a hemodynamic modeling on 10 healthy subjects and assessed the impact of using each of these imaging modalities as inlet boundary condition onto the simulated velocities over the carotid artery. We observed that the US-Doppler generally leads to higher velocity values compared to PC-MRI, which has also been quoted in other publications. PC-MRI data analysis showed velocity across the section of the artery follows a parabolic profile except in the sinus region. Overall, we found numerical velocities based on PC-MRI velocity inlet closer to measurements than those based on Doppler-US velocity inlet. Therefore, from our experiments, the PC-MRI-based hemodynamic modeling approach could be reasonably more realistic. As a future work, the improvement of the modeling approach is still required to better fit the measurements at peak systole and end diastole. In addition, we further aim to establish transfer functions between US, PC-MRI and simulated velocities in order to i) find from a given numerical velocity distribution the corresponding measured (US and/or PC-MRI) one, ii) provide reliable simulated profiles from limited information, such as anatomical MRI and US velocity inlet, or 3D-US [6] and US velocity inlet.

6. Appendix

Table 1
Anatomical measurements of studied patient-specific carotid artery models. ID refers to subject number. CCA: Common Carotid Artery, ECA: External Carotid Artery, ICA: Internal Carotid Artery, D_x: section diameter according to x, D_y: section diameter according to y.

ID	Artery	Inlet/outlet surface diameter (mm)	Vessel length(mm)	Inlet/outlet surface area (mm^2)	Total wall legth (mm^2)	Total surface area (mm^2)
	CCA	D_x=5.8, D_y=5.2	33	24.9		
1	ECA	D_x=2.5, D_y=2.3	25	4.8	58	1293
	ICA	D_x=4.4, D_y=3.8	25	13.7		
	CCA	D_x=5.7, D_y=5.5	33	26		
2	ECA	D_x=2.9, D_y=2.8	25	6.7	58	1445.7
	ICA	D_x=4.4, D_y=4.2	25	15.1		
	CCA	D_x=7, D_y=6.4	33	35.7		
3	ECA	D_x=3.2, D_y=2.9	25	7.6	58	1618.4
	ICA	D_x=4.5, D_y=4.4	25	16.1		
	CCA	D_x=5.6, D_y=5.2	33	23.4		
4	ECA	D_x=3, D_y=2.9	25	7	58	1223
	ICA	D_x=3.9, D_y=3.4	25	10.7		
	CCA	D_x=5.3, D_y=4.8	33	21		
5	ECA	D_x=4.2, D_y=3.9	25	12.9	58	1521.7
	ICA	D_x=4.2, D_y=3.9	25	13.2		
	CCA	D_x=6.4, D_y=5.8	33	29.5		
6	ECA	D_x=2.8, D_y=2.7	25	6.4	58	1477.3
	ICA	D_x=4.5, D_y=4	25	14.7		
	CCA	D_x=6.5, D_y=6.2	33	32.2		
7	ECA	D_x=25, D_y=18.7	25	11.3	58	1664.4
	ICA	D_x=5.3, D_y=4.3	25	14.7		
	CCA	D_x=5.5, D_y=5	33	22.3		
8	ECA	D_x=2.3, D_y=2.1	25	3.9	58	1259.8
	ICA	D_x=4.2, D_y=3.6	25	11.8		
	CCA	D_x=6.2, D_y=5.6	33	28		
9	ECA	D_x=3.7, D_y=3.9	25	11.5	58	1432.9
	ICA	D_x=4.5, D_y=4.1	25	14.7		
	CCA	D_x=6, D_y=5.4	33	26		
10	ECA	D_x=3.2, D_y=3.5	25	9.2	58	1231.3
	ICA	D_x=3.8, D_y=3.3	25	9.9		

Algorithm 1 Velocity extraction from PC-MR images during a cardiac cycle at a given pixel

Input: PC-MR images throughout a cardiac cycle
r, c: number of PC-MRI rows and columns, respectively
n: number of instants during a cardiac cycle
$RescaleSlope$, $RescaleIntercept$: specific DICOM fields which define linear subset of a conceptual Modality LUT transformation. These attributes are in relationship between stored values and output values
Output: Velocity at a given pixel location P(x,y) throughout a cardiac cycle

- Define the pixel coordinate $P(x, y)$
- Switch rows with columns: $P'(x, y) \leftarrow P(y, x)$
- Let C and V two matrices of size $r \bullet c$
- Declare a vector V_{pixel} of n elements

for i=1 to n **do**
$C \leftarrow image[i]$
Read C
$V \leftarrow m * C + b$
Where $m = RescaleSlope$ and $b = RescaleIntercept$
$V_{pixel}[i] = V[P'(x, y)]$
end for

Table 2
Measured peak systolic and end diastolic velocities V_{MRImax}, $V_{MRImean}$, V_{US}, compared to the estimated ones V_{SIMMRI} through CFD simulation in CCA for the ten subjects (V_{MRImax} and $V_{MRImean}$ values are obtained within a 3x3 window).

CCA	PC-MRI				US		Simulation			
Subject ID	*VMRImax (cm/s)*		*VMRImean (cm/s)*		*VUS (cm/s)*		*VSIM_MRImax (cm/s)*		*VSIM_US (cm/s)*	
	PSV*	EDV**	PSV*	EDV**	PSV*	EDV**	PSV*	EDV**	PSV*	EDV**
1	69.8	34	55.1	27.9	70	19.2	38.8	19.7	44.4	12
2	53.2	22	48.3	14.8	100	24.5	39.1	12.8	51.5	12.6
3	54.2	16.8	46.9	11.1	66.6	13.8	44.9	11.5	40.3	8.3
4	50.7	25.2	44.7	20.6	69.1	31.9	37	17.5	43.4	20
5	88.8	24.2	74.9	16.7	79.4	16.6	57.6	16.7	44.2	9.6
6	47.2	14.9	40.1	7.6	88.5	21.7	37.5	13.0	50.4	12.3
7	52.6	19.4	46	15.2	59.4	14.2	32	11.8	35.2	8.4
8	61.6	24.2	56.7	19.2	95	24	34.3	11	52.6	13.3
9	57.6	20.6	51.2	13.4	93	27	33.3	15.5	53.4	15.5
10	75.3	31.7	66.1	25.9	108	33.2	52.7	25.6	67.4	20.7
Mean ± SD	61 ± 13	23.3 ± 6	53 ± 10	17.2 ± 6	83 ± 16	22.6 ± 6	42 ± 9	15.5 ± 4	48.3 ± 8	13.3 ± 4

*PSV: Peak Systolic Velocity, **EDV End Diastolic Velocity

Table 3
Measured peak systolic and end diastolic velocities V_{MRImax}, $V_{MRImean}$, V_{US}, compared to the estimated ones V_{SIMMRI} through CFD simulation in ECA for the ten subjects (V_{MRImax} and $V_{MRImean}$ values are obtained within a 3x3 window).

ECA	PC-MRI				US		Simulation			
Subject ID	*VMRImax (cm/s)*		*VMRImean (cm/s)*		*VUS (cm/s)*		*VSIM_MRImax (cm/s)*		*VSIM_US (cm/s)*	
	PSV*	EDV**	PSV*	EDV**	PSV*	EDV**	PSV*	EDV**	PSV*	EDV**
1	32.1	16.2	26.3	12.12	106.1	20.6	38.2	19.4	44.4	11
2	36.1	13	31.3	7.35	112.5	23.4	45.3	11.9	47.7	11.6
3	95.8	40.7	47.5	15.82	90.8	12	61.2	15.3	49.4	10.2
4	36.3	11	27.4	5.74	129.5	43	40	18.9	46.8	21.6
5	65.4	22.3	55.7	14.48	83.8	22	36.9	11.6	30.9	6.4
6	25.1	11.8	19.1	4.93	65.5	15	28.4	9.9	38.1	9.3
7	45.9	16.2	32.1	7.23	108	13.1	21.4	7.9	23.5	5.6
8	30.1	13.5	26.2	5.99	101.3	40.3	28.3	9.1	43.4	10.9
9	49.6	18.4	36.9	12.35	100.4	39.4	27	6.5	43.3	6.5
10	62.9	24.2	48.7	15.7	118.5	20.5	46	22.3	58.8	18.1
Mean ± SD	48 ± 21	18.7 ± 8	35 ± 11	10 ± 4	101.6 ± 18	24.8 ± 11	36 ± 11	13 ± 5	42.6 ± 9	11 ± 5

*PSV: Peak Systolic Velocity, **EDV End Diastolic Velocity

Table 4
Measured peak systolic and end diastolic velocities V_{MRImax}, $V_{MRImean}$, V_{US}, compared to the estimated ones V_{SIMMRI} through CFD simulation in ICA for the ten subjects (V_{MRImax} and $V_{MRImean}$ values are obtained within a 3x3 window).

ICA	PC-MRI				US		Simulation			
Subject ID	*VMRImax (cm/s)*		*VMRImean (cm/s)*		*VUS (cm/s)*		*VSIM_MRImax (cm/s)*		*VSIM_US (cm/s)*	
	PSV*	EDV**	PSV*	EDV**	PSV*	EDV**	PSV*	EDV**	PSV*	EDV**
1	30.6	25.1	26.5	15.1	113.4	41.6	31.8	16.1	29.7	8.6
2	29	17.5	22.7	13.7	76.2	31	34.3	13.5	54.2	13.2
3	32.1	14.3	25	9.7	83.6	29.2	41.6	10.7	33.1	6.8
4	50.8	30.5	46.3	23.6	72	24.8	49	23.2	57.5	26.6
5	42.2	21	32.9	12.7	72.6	29.2	67.2	23	60.9	12.7
6	46.2	28.9	35.6	20.5	72.6	33	35.1	12.2	47	11.5
7	19.9	11.1	14.6	6.9	62.9	39.2	27.5	10.2	30.3	7.2
8	36.7	22.6	32.9	18	88.5	18.3	35.3	11.4	54.2	13.6
9	32.7	14.2	26.7	8.8	72.9	30	31.2	7.5	50.1	12.3
10	36.3	28.8	29	18.3	87.6	34	49.2	23.9	63	19.4
Mean ± SD	35.6 ± 9	21.4 ± 6	29.2 ± 8	14.7 ± 5	77.2 ± 15	29.2 ± 9	40.2 ± 11	15.1 ± 6	48 ± 12	13.2 ± 6

*PSV: Peak Systolic Velocity, **EDV End Diastolic Velocity

Table 5
Global and local indicators of similarity between measured and numerical velocities in CCA for the 10 volunteers.

CCA	V_{SIM_MRImax}			V_{SIM_US}		
Subject ID	$\varepsilon_v(\%)$	$\gamma_{PSV}(\%)$	$\gamma_{EDV}(\%)$	$\varepsilon_v(\%)$	$\gamma_{PSV}(\%)$	$\gamma_{EDV}(\%)$
1	24	44	42	16	7	13
2	18	26	41	22	48	48
3	8	17	31	14	39	39
4	20	27	30	19	37	37
5	17	35	31	17	44	41
6	15	20	12	19	43	43
7	17	39	38	18	4	40
8	26	44	54	19	44	44
9	21	42	24	19	42	42
10	15	35	17	15	37	37
Average ± SD	18.1 ± 5	32 ± 9	32 ± 12	17.8 ± 2	38 ± 11	38 ± 9

Table 6
Global and local indicators of similarity between measured and numerical velocities in ECA for the 10 volunteers.

ECA	V_{SIM_MRImax}			V_{SIM_US}		
Subject ID	$\varepsilon_v(\%)$	$\gamma_{PSV}(\%)$	$\gamma_{EDV}(\%)$	$\varepsilon_v(\%)$	$\gamma_{PSV}(\%)$	$\gamma_{EDV}(\%)$
1	13	19	19	27	58	46
2	9	25	8	20	57	50
3	19	36	62	7	45	14
4	8	10	72	37	63	49
5	14	43	47	26	63	70
6	11	13	16	18	41	37
7	22	53	51	24	78	56
8	7	5	32	44	75	72
9	19	45	64	41	56	72
10	15	26	7	18	5	11
Average ± SD	13.7 ± 5	27 ± 16	37 ± 24	26.2 ± 11	58 ± 11	47 ± 21

Table 7
Global and local indicators of similarity between measured and numerical velocities in ICA for the 10 volunteers.

ICA	V_{SIM_MRImax}			V_{SIM_US}		
Subject ID	$\varepsilon_v(\%)$	$\gamma_{PSV}(\%)$	$\gamma_{EDV}(\%)$	$\varepsilon_v(\%)$	$\gamma_{PSV}(\%)$	$\gamma_{EDV}(\%)$
1	16	3	35	27	73	79
2	22	18	22	11	28	57
3	13	9	25	40	60	76
4	21	3	23	7	20	7
5	38	58	9	27	16	56
6	29	24	57	29	35	65
7	12	44	8	29	51	81
8	30	3	49	12	38	10
9	26	4	47	22	31	58
10	17	35	17	29	28	42
Average ± SD	22 ± 8	22 ± 19	29 ± 17	23 ± 10	38 ± 18	53 ± 26

References

[1] Adib, M.A.H.M., Ii, S., Watanabe, Y., Wada, S., 2017. Minimizing the blood velocity differences between phase-contrast magnetic resonance imaging and computational fluid dynamics simulation in cerebral arteries and aneurysms. Medical & biological engineering & computing 55, 1605–1619.

[2] Ahmed, S.A., Giddens, D.P., 1984. Pulsatile poststenotic flow studies with laser doppler anemometry. Journal of biomechanics 17, 695–705.

[3] Alastruey, J., Khir, A.W., Matthys, K.S., Segers, P., Sherwin, S.J., Verdonck, P.R., Parker, K.H., Peiró, J., 2011. Pulse wave propagation in a model human arterial network: assessment of 1-d visco-elastic simulations against in vitro measurements. Journal of biomechanics

44, 2250–2258.

[4] Ben Abdallah, A., Debbich, A., 2017. Effect of surface re-meshing on hemodynamic simulations quality in carotid arteries, in: 2017 IEEE/ACS 14th International Conference on Computer Systems and Applications (AICCSA), IEEE. pp. 334–341.

[5] Bland, J.M., Altman, D., 1986. Statistical methods for assessing agreement between two methods of clinical measurement. The lancet 327, 307–310.

[6] Calogero, E., Fabiani, I., Pugliese, N.R., Santini, V., Ghiadoni, L., Di Stefano, R., Galetta, F., Sartucci, F., Penno, G., Berchiolli, R., et al., 2018. Three-dimensional echographic evaluation of carotid artery disease. Journal of cardiovascular echography 28, 218.

[7] Campbell, I.C., Ries, J., Dhawan, S.S., Quyyumi, A.A., Taylor, W.R., Oshinski, J.N., 2012. Effect of inlet velocity profiles on patient-specific computational fluid dynamics simulations of the carotid bifurcation. Journal of biomechanical engineering 134, 051001.

[8] Cebral, J.R., Yim, P.J., Löhner, R., Soto, O., Choyke, P.L., 2002. Blood flow modeling in carotid arteries with computational fluid dynamics and mr imaging. Academic radiology 9, 1286–1299.

[9] Debbich, A., Abdallah, A.B., 2017. Blood flow modeling in a healthy carotid artery bifurcation: simulations against in vivo measurements, in: 2017 IEEE/ACS 14th International Conference on Computer Systems and Applications (AICCSA), IEEE. pp. 69–70.

[10] Dong, J., Inthavong, K., Tu, J., 2013a. Image-based computational hemodynamics evaluation of atherosclerotic carotid bifurcation models. Computers in biology and medicine 43, 1353–1362.

[11] Dong, J., Wong, K.K., Tu, J., 2013b. Hemodynamics analysis of patient-specific carotid bifurcation: A cfd model of downstream peripheral vascular impedance. International journal for numerical methods in biomedical engineering 29, 476–491.

[12] Gijsen, F.J., van de Vosse, F.N., Janssen, J., 1999. The influence of the non-newtonian properties of blood on the flow in large arteries: steady flow in a carotid bifurcation model. Journal of biomechanics 32, 601–608.

[13] Hanning, U., Sporns, P.B., Schmiedel, M., Ringelstein, E.B., Heindel, W., Wiendl, H., Niederstadt, T., Dittrich, R., 2017. Ct versus mr techniques in the detection of cervical artery dissection. Journal of Neuroimaging 27, 607–612.

[14] Harloff, A., Albrecht, F., Spreer, J., Stalder, A., Bock, J., Frydrychowicz, A., Schöllhorn, J., Hetzel, A., Schumacher, M., Hennig, J., et al., 2009. 3d blood flow characteristics in the carotid artery bifurcation assessed by flow-sensitive 4d mri at 3t. Magnetic Resonance in Medicine: An Official Journal of the International Society for Magnetic Resonance in Medicine 61, 65–74.

[15] Harloff, A., Zech, T., Wegent, F., Strecker, C., Weiller, C., Markl, M., 2013. Comparison of blood flow velocity quantification by 4d flow mr imaging with ultrasound at the carotid bifurcation. American Journal of Neuroradiology 34, 1407–1413.

[16] Holbek, S., Hansen, K.L., Bouzari, H., Ewertsen, C., Stuart, M.B., Thomsen, C., Nielsen, M.B., Jensen, J.A., 2017. Common carotid artery flow measured by 3-d ultrasonic vector flow imaging and validated with magnetic resonance imaging. Ultrasound in medicine & biology 43, 2213–2220.

[17] Holdsworth, D., Norley, C., Frayne, R., Steinman, D., Rutt, B., 1999. Characterization of common carotid artery blood-flow waveforms in normal human subjects. Physiological measurement 20, 219.

[18] Jensen, J., Hoyos, C.A.V., Traberg, M.S., Olesen, J.B., Tomov, B.G., Moshavegh, R., Holbek, S., Stuart, M.B., Ewertsen, C., Hansen, K.L., et al., 2018. Accuracy and precision of a plane wave vector flow imaging method in the healthy carotid artery. Ultrasound in medicine & biology 44, 1727–1741.

[19] Jonášová, A., Vimmr, J., 2018. Noninvasive assessment of carotid artery stenoses by the principle of multiscale modelling of non-newtonian blood flow in patient-specific models. Applied Mathematics and Computation 319, 598–616.

[20] Kallinderis, Y., Khawaja, A., McMorris, H., 1996. Hybrid prismatic/tetrahedral grid generation for viscous flows around complex geometries. AIAA journal 34, 291–298.

[21] Kefayati, S., Poepping, T.L., 2013. Transitional flow analysis in the carotid artery bifurcation by proper orthogonal decomposition and particle image velocimetry. Medical engineering & physics 35, 898–909.

[22] Kenjereš, S., 2016. On recent progress in modelling and simulations of multi-scale transfer of mass, momentum and particles in biomedical applications. Flow, Turbulence and Combustion 96, 837–860.

[23] Kenjereš, S., de Loor, A., 2014. Modelling and simulation of low-density lipoprotein transport through multi-layered wall of an anatomically realistic carotid artery bifurcation. Journal of The Royal Society Interface 11, 20130941.

[24] Kochanowicz, J., Turek, G., Rutkowski, R., Mariak, Z., Szydlik, P., Lyson, T., Krejza, J., 2009. Normal reference values of ratios of blood flow velocities in internal carotid artery to those in common carotid artery using doppler sonography. Journal of Clinical Ultrasound 37, 208–211.

[25] Koltukluoğlu, T.S., Blanco, P.J., 2018. Boundary control in computational haemodynamics. Journal of Fluid Mechanics 847, 329–364.

[26] Ku, D.N., 1997. Blood flow in arteries. Annual review of fluid mechanics 29, 399–434.

[27] Lorensen, W.E., Cline, H.E., 1987. Marching cubes: A high resolution 3d surface construction algorithm, in: ACM siggraph computer graphics, ACM. pp. 163–169.

[28] Maier, I.L., Hofer, S., Joseph, A.A., Merboldt, K.D., Tan, Z., Schregel, K., Knauth, M., Bähr, M., Psychogios, M.N., Liman, J., et al., 2018. Carotid artery flow as determined by real-time phase-contrast flow mri and neurovascular ultrasound: A comparative study of healthy subjects. European journal of radiology 106, 38–45.

[29] Mark, M., Baurzhan, M., Tobias, W., et al., . Engauge digitizer software. URL: http://markummitchell.github.io/engauge-digitizer, LastAccessed:September23,2019.

[30] Markl, M., Frydrychowicz, A., Kozerke, S., Hope, M., Wieben, O., 2012. 4d flow mri. Journal of Magnetic Resonance Imaging 36, 1015–1036.

[31] Marshall, I., Papathanasopoulou, P., Wartolowska, K., 2004. Carotid flow rates and flow division at the bifurcation in healthy volunteers. Physiological measurement 25, 691.

[32] Morbiducci, U., Gallo, D., Massai, D., Consolo, F., Ponzini, R., Antiga, L., Bignardi, C., Deriu, M.A., Redaelli, A., 2010. Outflow conditions for image-based hemodynamic models of the carotid bifurcation: implications for indicators of abnormal flow. Journal of biomechanical engineering 132, 091005.

[33] Morbiducci, U., Gallo, D., Massai, D., Ponzini, R., Deriu, M.A., Antiga, L., Redaelli, A., Montevecchi, F.M., 2011. On the importance of blood rheology for bulk flow in hemodynamic models of the carotid bifurcation. Journal of biomechanics 44, 2427–2438.

[34] Moyle, K.R., Antiga, L., Steinman, D.A., 2006. Inlet conditions for image-based cfd models of the carotid bifurcation: is it reasonable to assume fully developed flow? Journal of biomechanical engineering 128, 371–379.

[35] Nagel, T., Resnick, N., Dewey Jr, C.F., Gimbrone Jr, M.A., 1999. Vascular endothelial cells respond to spatial gradients in fluid shear stress by enhanced activation of transcription factors. Arteriosclerosis, thrombosis, and vascular biology 19, 1825–1834.

[36] Nemati, M., Loozen, G., Van der Wekken, N., Van de Belt, G., Urbach, H., Bhattacharya, N., Kenjeres, S., 2015. Application of full field optical studies for pulsatile flow in a carotid artery phantom. Biomedical optics express 6, 4037–4050.

[37] Perktold, K., Resch, M., 1990. Numerical flow studies in human carotid artery bifurcations: basic discussion of the geometric factor in atherogenesis. Journal of Biomedical Engineering 12, 111–123.

[38] Pinter, S., Jachowski, J., Rubin, J.M., Fowlkes, J.B., Younger, J., Kripfgans, O., 2015. 2091330 volumetric carotid blood flow assessment-a comparison of us and mri. Ultrasound in Medicine and Biology 41, S75.

[39] Piskin, S., Celebi, M.S., 2013. Analysis of the effects of different pulsatile inlet profiles on the hemodynamical properties of blood flow

in patient specific carotid artery with stenosis. Computers in biology and medicine 43, 717–728.

[40] Rahman, M.M., Hossain, M.A., Mamun, K., Akhter, M.N., 2017. Comparative study of newtonian physiological blood flow through normal and stenosed carotid artery, in: AIP Conference Proceedings, AIP Publishing. p. 020047.

[41] Rispoli, V.C., Nielsen, J.F., Nayak, K.S., Carvalho, J.L., 2015. Computational fluid dynamics simulations of blood flow regularized by 3d phase contrast mri. Biomedical engineering online 14, 110.

[42] Ritchie, H., Roser, M., 2013. Cause of death. Our World in Data .

[43] Russin, J., Babiker, H., Ryan, J., Rangel-Castilla, L., Frakes, D., Nakaji, P., 2015. Computational fluid dynamics to evaluate the management of a giant internal carotid artery aneurysm. World neurosurgery 83, 1057–1065.

[44] Saqr, K.M., Mansour, O., Tupin, S., Hassan, T., Ohta, M., 2019. Evidence for non-newtonian behavior of intracranial blood flow from doppler ultrasonography measurements. Medical & biological engineering & computing 57, 1029–1036.

[45] Seong, J., Jeong, W., Smith, N., Towner, R.A., 2015. Hemodynamic effects of long-term morphological changes in the human carotid sinus. Journal of biomechanics 48, 956–962.

[46] Sousa, L.C., Castro, C.F., António, C.C., Santos, A.M.F., dos Santos, R.M., Castro, P.M.A., Azevedo, E., Tavares, J.M.R., 2014. Toward hemodynamic diagnosis of carotid artery stenosis based on ultrasound image data and computational modeling. Medical & biological engineering & computing 52, 971–983.

[47] Stankovic, Z., Allen, B.D., Garcia, J., Jarvis, K.B., Markl, M., 2014. 4d flow imaging with mri. Cardiovascular diagnosis and therapy 4, 173.

[48] Sutton-Tyrrell, K., Alcorn, H.G., Wolfson Jr, S.K., Kelsey, S.F., Kuller, L.H., 1993. Predictors of carotid stenosis in older adults with and without isolated systolic hypertension. Stroke 24, 355–361.

[49] Szajer, J., Ho-Shon, K., 2018. A comparison of 4d flow mri-derived wall shear stress with computational fluid dynamics methods for intracranial aneurysms and carotid bifurcations—a review. Magnetic resonance imaging 48, 62–69.

[50] Tan, F., Soloperto, G., Bashford, S., Wood, N., Thom, S., Hughes, A., Xu, X., 2008. Analysis of flow disturbance in a stenosed carotid artery bifurcation using two-equation transitional and turbulence models. Journal of biomechanical engineering 130, 061008.

[51] Valant, A.Z., Ziberna, L., Papaharilaou, Y., Anayiotos, A., Georgiou, G.C., 2016. The influence of oxygen concentration on the rheological properties and flow of whole human blood. Rheologica Acta 55, 921–933.

[52] Wang, J., Paritala, P.K., Mendieta, J.B., Komori, Y., Raffel, O.C., Gu, Y., Li, Z., 2019. Optical coherence tomography-based patient-specific coronary artery reconstruction and fluid–structure interaction simulation. Biomechanics and modeling in mechanobiology , 1–14.

[53] Weatherill, N.P., 1992. Delaunay triangulation in computational fluid dynamics. Computers & Mathematics with Applications 24, 129–150.

[54] Wetzel, S., Meckel, S., Frydrychowicz, A., Bonati, L., Radue, E.W., Scheffler, K., Hennig, J., Markl, M., 2007. In vivo assessment and visualization of intracranial arterial hemodynamics with flow-sensitized 4d mr imaging at 3t. American Journal of Neuroradiology 28, 433–438.

[55] Willemet, M., Lacroix, V., Marchandise, E., 2013. Validation of a 1d patient-specific model of the arterial hemodynamics in bypassed lower-limbs: simulations against in vivo measurements. Medical engineering & physics 35, 1573–1583.